

1
2
3
4
5
6
7
8
9
10
11
12
13
14
15
16
17
18
19
20
21
22
23
24
25
26
27
28
29
30
31
32
33
34
35
36
37
38
39
40
41
42
43
44
45
46
47
48
49
50
51
52
53
54
55
56
57
58
59
60
61
62
63
64
65

Robust membrane detection based on tensor voting for electron tomography

Antonio Martinez-Sanchez^a, Inmaculada Garcia^b, Shoh Asano^c, Vladan Lucic^c,
Jose-Jesus Fernandez^{d,*}

^a*Supercomputing and algorithms group. Associated Unit CSIC-UAL, Universidad de Almeria,
04120 Almeria, Spain*

^b*Supercomputing and algorithms group. Dept. Computer architecture. Universidad de Malaga,
29080 Malaga, Spain*

^c*Max-Planck Institute of Biochemistry, Am Klopferspitz 18, 82152 Martinsried, Germany*

^d*National Centre for Biotechnology. National Research Council (CNB-CSIC). Campus UAM.
Darwin 3. Cantoblanco. 28049 Madrid. Spain.*

*Corresponding author:
National Centre for Biotechnology.
National Research Council (CNB-CSIC).
Campus UAM. C/ Darwin 3. Cantoblanco.
28049 Madrid. Spain.
Tel: +34 91 585 4619. Fax: +34 91 585 4506
Email: jj.fernandez@csic.es

Preprint submitted to J. Struct. Biol.

February 20, 2014

1
2
3
4
5
6
7
8
9
10
11
12
13
14
15
16
17
18
19
20
21
22
23
24
25
26
27
28
29
30
31
32
33
34
35
36
37
38
39
40
41
42
43
44
45
46
47
48
49
50
51
52
53
54
55
56
57
58
59
60
61
62
63
64
65

Abstract

Electron tomography enables three-dimensional (3D) visualization and analysis of the subcellular architecture at a resolution of a few nanometres. Segmentation of structural components present in 3D images (tomograms) is often necessary for their interpretation. However, it is severely hampered by a number of factors that are inherent to electron tomography (e.g. noise, low contrast, distortion). Thus, there is a need for new and improved computational methods to facilitate this challenging task. In this work, we present a new method for membrane segmentation that is based on anisotropic propagation of the local structural information using the Tensor Voting algorithm. The local structure at each voxel is then refined according to the information received from other voxels. Because voxels belonging to the same membrane have coherent structural information, the underlying global structure is strengthened. In this way, local information is easily integrated at a global scale to yield segmented structures. This method performs well under low signal-to-noise ratio typically found in tomograms of vitrified samples under cryo-tomography conditions and can bridge gaps present on membranes. The performance of the method is demonstrated by applications to tomograms of different biological samples and by quantitative comparison with standard template matching procedure.

1
2
3
4
5
6
7
8
9
10
11
12
13
14
15
16
17
18
19
20
21
22
23
24
25
26
27
28
29
30
31
32
33
34
35
36
37
38
39
40
41
42
43
44
45
46
47
48
49
50
51
52
53
54
55
56
57
58
59
60
61
62
63
64
65

Keywords

Segmentation , Image Processing , Electron Tomography , Membrane , Tensor
Voting , Steerable Filters

1
2
3
4
5
6
7
8
9 **1. Introduction**

10
11
12 Electron tomography (ET) enables three-dimensional (3D) visualization and
13 analysis of the subcellular architecture and macromolecular organization of cells
14 and tissues in situ at a resolution of a few nanometers (Lucic et al., 2013). This
15 technique involves the acquisition of electron microscopy projection images of a
16 specimen at different orientations. These images are then combined by means of
17 tomographic reconstruction methods to yield the 3D volume (Fernandez, 2012).
18
19
20
21
22

23
24 Segmentation of the 3D volume into its constitutive structural elements is key
25 for their interpretation. However, it proves to be challenging because of a number
26 of factors such as the crowded cellular environment, the distortion caused by the
27 missing wedge and noise, which is particularly high in ET of fully hydrated and
28 vitrified samples (cryo-ET) (Volkman, 2010; Fernandez, 2012). Thus, segmen-
29 tation constitutes a major bottleneck in ET, especially in those studies intended
30 to visualize the subcellular architecture under cryo-conditions. Although several
31 computational segmentation methods have been presented, none has shown gen-
32 eral applicability yet. As a consequence, manual segmentation is still a method of
33 choice.
34
35
36
37
38
39
40
41
42

43
44 Software packages often used in ET have been gradually including segmen-
45 tation procedures based on the most known computational techniques (Water-
46 shed transform and thresholding (Volkman, 2002; Cyrklaff et al., 2005)). This
47 makes segmentation a semi-automatic process, thus facilitating its use. In the
48 last several years, there have been significant advances towards computational de-
49 tection of specific structural features within tomograms, like membranous struc-
50 tures, filaments and microtubules (Lebbink et al., 2007; Sandberg and Brega,
51 2007; Moussavi et al., 2010; Nurgaliev et al., 2010; Rigort et al., 2012; Weber
52
53
54
55
56
57
58
59
60
61
62
63
64
65

1
2
3
4
5
6
7
8
9 [et al., 2012](#)). Many of these methods rely on some sort of template matching.
10 That is, they search for a template that is suited to the targeted feature, typi-
11 cally by means of cross-correlation techniques. In contrast to these methods, we
12 have recently developed a differential geometry-based segmentation that is par-
13 ticularly suited for membranes ([Martinez-Sanchez et al., 2011, 2013](#)). We first
14 proposed a method that uses a local membrane detector based on the Hessian
15 tensor ([Martinez-Sanchez et al., 2011](#)). Later, we improved this detector and ex-
16 tended the abilities of the framework to characterize and classify the detected
17 membranous structures ([Martinez-Sanchez et al., 2013](#)). Nevertheless, this local
18 membrane detector still presented several limitations. Namely, gaps that may ap-
19 pear on membranes due to experimental imaging conditions were not properly
20 filled. Also, membrane-attached structures were not discarded and were instead
21 segmented as part of the membranes. A non-trivial postprocessing stage was re-
22 quired in these cases to actually extract the membrane voxels. Finally, the detector
23 used was suitable for membranes with ridge-like (i.e. local maximum) profile, and
24 was therefore unable to identify edge-like structures (e.g. membrane of vesicles
25 having dense interior).

26
27
28
29
30
31
32
33
34
35
36
37
38
39
40
41 In this work, we propose a more robust local membrane detector. The method
42 is based on broadcasting differential information through the 3D space using the
43 Tensor Voting algorithm ([Tong et al., 2004](#)). In this way, nearby voxels that belong
44 to the same membranous structure enhance each other’s structural information. As
45 a result, the new local detector can fill the gaps present on membranes, disregards
46 structures apposed to the membranes, and it is more robust against low signal-to-
47 noise ratio, thus simplifying the postprocessing stage. In this work we also show
48 that membranes having ridge-like and edge-like profiles can be detected using the
49
50
51
52
53
54
55
56
57
58
59
60
61
62
63
64
65

1
2
3
4
5
6
7
8
9 same procedure but different tensor that provides the differential information.

10 11 **2. Background on local membrane detection**

12 13 *2.1. Hessian tensor-based detection*

14
15 It is assumed that, at a local scale, a membrane can be modelled as a plane-
16 like structure with membrane density profile (in the direction perpendicular to
17 the membrane) following a Gaussian function. That is, the membrane profile is
18 ridge-like, its density decreases as a function of the distance from the center of the
19 membrane.
20
21
22
23
24
25

26 Membrane detection starts with the application of a scale-space operation on a
27 greyscale volume, typically implemented as Gaussian low-pass filtering. This step
28 is used to isolate the information at a given scale σ , thus filtering out noise and
29 all features smaller than the scale. An additional benefit of this step is that scale-
30 space can smooth membranes making their profile closer to Gaussian. Typically,
31 σ is set to the thickness (expressed in voxels) of the targeted membrane (Martinez-
32 Sanchez et al., 2011).
33
34
35
36
37
38

39 Previously, our local detector for ridge-like membranes was based on the Hes-
40 sian tensor (Martinez-Sanchez et al., 2011). This tensor provides information
41 about the second order density variation, as it is defined as:
42
43
44
45

$$46 \quad \mathbf{H} = \begin{bmatrix} \frac{\partial^2 L}{\partial x^2} & \frac{\partial^2 L}{\partial x \partial y} & \frac{\partial^2 L}{\partial x \partial z} \\ \frac{\partial^2 L}{\partial x \partial y} & \frac{\partial^2 L}{\partial y^2} & \frac{\partial^2 L}{\partial y \partial z} \\ \frac{\partial^2 L}{\partial x \partial z} & \frac{\partial^2 L}{\partial y \partial z} & \frac{\partial^2 L}{\partial z^2} \end{bmatrix} \quad (1)$$

47
48 where L denotes the volume after the scale-space operation and $\frac{\partial^2 L}{\partial i \partial j} \forall i, j \in (x, y, z)$
49 are its second order partial derivatives. As a result of the eigen-analysis of the
50
51
52
53
54
55
56
57
58
59
60
61
62
63
64
65

Hessian tensor, three orthogonal eigenvectors \vec{v}_i and their corresponding eigenvalues λ_i (representing second order derivatives along \vec{v}_i) are obtained, which characterize the local structure around any voxel of the volume. If we assume $|\lambda_1| > |\lambda_2| > |\lambda_3|$, then the first eigenvector \vec{v}_1 , i.e. the one whose eigenvalue exhibits the largest absolute value, points to the direction of the maximum curvature. If the local structure is a plane, \vec{v}_1 points to the direction perpendicular to the plane and the following relationship holds $|\lambda_1| \gg |\lambda_2| \approx |\lambda_3|$. This led us earlier to propose a local detector (so-called membrane strength, M) defined as follows (Martinez-Sanchez et al., 2011):

$$M = \begin{cases} \frac{(|\lambda_1| - \sqrt{\lambda_2 \lambda_3})^2}{|\nabla L|^2} & \lambda_1 < 0 \\ 0 & \text{otherwise} \end{cases} \quad (2)$$

where $|\nabla L|$ denotes the gradient of the volume L resulting from the scale-space operation.

We used two additional steps to detect peaks of M corresponding to membranes. A threshold t_M over M was imposed to select membrane-like voxels. This was then coupled with the non-maximum suppression (NMS) criterion which selects only the ridge points (i.e. the local maxima in the direction perpendicular to the membrane). The use of NMS results in detected membranes being represented as one-voxel thick surfaces in the 3D space. In summary, the local detector for ridge-like membranes is given by the following equation (Martinez-Sanchez et al., 2013), where the first condition represents NMS, δ is a small number and $\mathbf{x} \in \mathbb{R}^3$ denotes a voxel of the volume:

$$\begin{cases} (L(\mathbf{x}) > L(\mathbf{x} - \delta\vec{v}_1)) \text{ and } (L(\mathbf{x}) > L(\mathbf{x} + \delta\vec{v}_1)) \\ M(\mathbf{x}) \geq t_M \end{cases} \quad (3)$$

1
2
3
4
5
6
7
8
9 2.2. *Structure tensor to detect edge-like membranes*

10
11 The detector defined in the previous section can detect ridge-like membranes,
12 but it is not suitable for the detection of membranes with edge-like profile where
13 density on one side of the membrane is similar to that of the membrane (e.g. those
14 presented by a densely filled vesicle). Consequently, a new detector for this type
15 of membranes is required. To this end, we focus our attention to the Structure
16 tensor (Weickert, 1998), also known as the second moment tensor, which is given
17 by:
18
19
20
21
22
23

$$24 \quad \mathbf{J} = \begin{bmatrix} \left(\frac{\partial L}{\partial x}\right)^2 & \frac{\partial L}{\partial x} \frac{\partial L}{\partial y} & \frac{\partial L}{\partial x} \frac{\partial L}{\partial z} \\ 25 & \frac{\partial L}{\partial x} \frac{\partial L}{\partial y} & \left(\frac{\partial L}{\partial y}\right)^2 & \frac{\partial L}{\partial y} \frac{\partial L}{\partial z} \\ 26 & \frac{\partial L}{\partial x} \frac{\partial L}{\partial z} & \frac{\partial L}{\partial y} \frac{\partial L}{\partial z} & \left(\frac{\partial L}{\partial z}\right)^2 \end{bmatrix} \quad (4)$$

27
28 where $\frac{\partial L}{\partial i} \forall i \in (x, y, z)$ are the first order derivatives of the scale-spaced volume
29 L . The eigen-analysis of this tensor proceeds as in the previous case (Fernandez
30 and Li, 2003, 2005). The first eigenvector \vec{v}_1 , i.e. the one whose eigenvalue ex-
31 hibits the largest value, points to the direction of the maximum variation. Also,
32 a local plane satisfies $|\lambda_1| \gg |\lambda_2| \approx |\lambda_3|$. However, the Hessian and Structure
33 tensors differ regarding the exact position of the detected surface. For a ridge pro-
34 file L , the local maximum of the largest eigenvalue ($|\lambda_1|$) of the Hessian tensor
35 corresponds to the maximum of L (Figure 1(Left)). For an edge profile L , the
36 local maximum of the largest eigenvalue ($|\lambda_1|$) of the Structure tensor corresponds
37 to the inflection point of L (Figure 1(Right)). Consequently, the Structure tensor
38 is well suited to detect edge-like local structures. Moreover, the output of this
39 edge detector is equivalent to the output of the Hessian-based detector (red curves
40 in Figure 1). This means that the eigen-analysis of the Structure tensor allows
41 detection of edges and their conversion into ridges. This, in turn, enables appli-
42
43
44
45
46
47
48
49
50
51
52
53
54
55
56
57
58
59
60
61
62
63
64
65

1
2
3
4
5
6
7
8
9 cation of all our ridge-based methodology to detect membranes with edge profile.
10 Therefore, the ridge-like profiles detected by the Hessian-based detector and the
11 edge-like profiles detected by the Structure tensor-based detector can be further
12 processed in the same way.
13
14

15
16 In this work, first and second order derivatives required for the components
17 of the tensors have been implemented based on central differences (Frangakis and
18 Hegerl, 2001).
19
20
21

22 23 **3. Tensor Voting** 24

25
26 In this section, the theoretical background on Tensor Voting (TV) is presented.
27 Our aim is to apply TV to enhance surface- or plane-like structures, such as mem-
28 branes in tomograms. In order to benefit from an efficient implementation of the
29 TV algorithm in 2D, and because of the high computational demands presented
30 by TV in 3D we chose to apply TV on tomographic slices. This is supported by
31 the fact that membranes in tomograms appear as curves in 2D planes (Martinez-
32 Sanchez et al., 2011). Thus, we proceed by using TV to detect curves on the slices.
33 In our procedure, TV is applied to all slices along all three major axes. Therefore,
34 in this section 2D TV algorithm and an efficient implementation of this algorithm
35 are presented.
36
37
38
39
40
41
42
43
44

45 46 *3.1. Introduction to Tensor Voting* 47

48 Tensor Voting is a technique used in computer vision for robust identifica-
49 tion of salient features, which exhibits excellent performance under particularly
50 challenging noise conditions (Medioni et al., 2000). In TV, voxels propagate in-
51 formation about their local structural features across their neighbourhood. The
52 local properties at each voxel are then refined according to the information re-
53
54
55
56
57
58

ceived from the neighbours. The aim is that voxels that belong to the same global feature (e.g. a surface or membrane in our case, **which are represented as curves in 2D**), and thus have coherent structural information, strengthen each other's contribution to the underlying global structure.

There are several important concepts and steps involved in TV: representation of the local structural information, the initialization of that information, the propagation through votes, the gathering of votes and refinement of the local information. They will be described in the following sections.

3.1.1. Data representation

In TV the local structural information at each voxel is represented by a symmetric non-negative definite second order tensor. This tensor allows encoding saliency of different types of geometric structures (**curves and blobs in the 2D case**) by its eigenvalues (λ_1 and λ_2 , with $\lambda_1 \geq \lambda_2 \geq 0$), and the corresponding eigenvectors (\vec{v}_1 and \vec{v}_2):

$$\mathbf{T} = \begin{bmatrix} t_{xx} & t_{xy} \\ t_{xy} & t_{yy} \end{bmatrix} = \begin{bmatrix} \vec{v}_1 & \vec{v}_2 \end{bmatrix} \begin{bmatrix} \lambda_1 & 0 \\ 0 & \lambda_2 \end{bmatrix} \begin{bmatrix} \vec{v}_1 & \vec{v}_2 \end{bmatrix}^T. \quad (5)$$

Geometric structures can be detected from this tensor as described in the previous section for the Structure tensor and Hessian tensor ([Fernandez and Li, 2003, 2005](#); [Martinez-Sanchez et al., 2011, 2013](#)), **but converted to the 2D case**. Thus, **voxels belonging to a local curve have $\lambda_1 \gg \lambda_2$, with \vec{v}_1 in the direction perpendicular to the curve, and the term $\lambda_1 - \lambda_2$ represents the curve saliency**. At voxels that do not show a clear structure (blob-like), the **two** eigenvalues have similar magnitude. The concept of saliency can be understood as the likelihood of a voxel to belong to one of the basic geometric features.

1
2
3
4
5
6
7
8
9 It is useful to decompose the tensor in order to reveal better the different types
10 of saliency as follows:
11

$$12 \quad \mathbf{T} = \lambda_1 \vec{v}_1 \vec{v}_1^T + \lambda_2 \vec{v}_2 \vec{v}_2^T = (\lambda_1 - \lambda_2) \vec{v}_1 \vec{v}_1^T + \lambda_2 (\vec{v}_1 \vec{v}_1^T + \vec{v}_2 \vec{v}_2^T) \quad (6)$$

13
14
15
16
17
18 In this decomposition, the **two** terms are called stick and ball components,
19 respectively (Medioni et al., 2000; Tong et al., 2004). In a voxel belonging to a
20 **curve**, the stick component dominates because of the high saliency $\lambda_1 - \lambda_2$. In the
21 extreme case: $\lambda_1 > 0$ and $\lambda_2 = 0$, so only the stick component remains. Such a
22 tensor is then referred to as stick tensor, and it encodes a pure **local curve** with
23 saliency λ_1 and the normal vector \vec{v}_1 .
24
25
26
27
28
29

30 Saliency of the stick component of a 2D tensor \mathbf{T} and the direction of the
31 corresponding vector with respect to the x-axis can be calculated analytically, as
32 follows (Franken et al., 2006):
33
34
35
36

$$37 \quad S(\mathbf{T}) = \lambda_1 - \lambda_2 = \sqrt{\text{tr}(\mathbf{T})^2 - 4 \det(\mathbf{T})} = \sqrt{(t_{xx} - t_{yy})^2 + 4t_{xy}^2} \quad (7)$$

$$38 \quad \alpha(\mathbf{T}) = \arccos(\vec{v}_1 \cdot \hat{e}_x) = \frac{1}{2} \arg(t_{xx} - t_{yy} + 2it_{xy}) \quad (8)$$

39
40
41 Here, $\text{tr}(\mathbf{T})$ and $\det(\mathbf{T})$ denote the trace and determinant of the matrix \mathbf{T} , respec-
42 tively, \cdot is the dot product, i represents the imaginary unit (i.e. $i^2 = -1$) and $\arg()$
43 is the phase of a complex number.
44
45
46
47
48
49

50 3.1.2. Initialization and generation of the input tensor field

51 Tensors in TV are typically initialized to isotropic balls (i.e. equal eigenval-
52 ues) or estimated from prior knowledge if available (Medioni et al., 2000; Tong
53 et al., 2004). In this work, we are interested in detecting **curve-like structures in**
54
55
56
57
58
59

the 2D tomographic slices. Thus, for each input 2D slice subjected to TV, Hessian or Structure tensors are calculated and the input tensor field is created as the pure stick component of the eigen-decomposition of the tensor field. Namely, the eigenvectors of the input tensor field are $\vec{v}_i, \forall i$, while the saliency is $|\lambda_1 - \lambda_2|$ so that:

$$\mathbf{T} = |\lambda_1 - \lambda_2| \vec{v}_1 \vec{v}_1^T \quad (9)$$

This defines an input tensor field $\mathbf{T}(\mathbf{x})$, with \mathbf{x} denoting the voxel coordinates, that represents the preliminary estimated likelihood of each voxel in the input slice to belong to a curve. Tensor Voting procedure refines the tensor information at each voxel by propagating the tensors to the neighbourhood, as presented in the following subsections.

3.1.3. Voting mechanism

Voxels communicate among themselves by propagating information between each other by a process called voting. The information passed is a second order tensor called vote, which is sent from a voter voxel to a receiver voxel. In this work, votes are based solely on stick tensors because they carry information about curves. A vote is propagated along an arc of a circle that contains voter \mathbf{x}' and receiver \mathbf{x} and is perpendicular to the vector that defines the orientation of the vote at the voter point (Figure 2(A)). The propagation of the vote from voter \mathbf{x}' to receiver \mathbf{x} induces the transformation of the stick tensor according to the so-called stick voting tensor field defined as follows (Medioni et al., 2000):

$$\mathbf{V}(\mathbf{x} - \mathbf{x}', \alpha(\mathbf{T}(\mathbf{x}'))) = e^{-\left(\frac{r^2 + dk^2}{\sigma_v^2}\right)} \vec{N} \vec{N}^T \quad (10)$$

1
2
3
4
5
6
7
8
9 where $s = s(\mathbf{x} - \mathbf{x}') = \frac{l\phi}{\sin\phi}$ is the length of the arc that connects the voter and the
10 receiver, $\kappa = \kappa(\mathbf{x} - \mathbf{x}') = \frac{2\sin\phi}{l}$ the curvature of the osculating circle, d a constant
11 that controls the decay with respect to curvature and σ_v is the length scale of anal-
12 ysis, which determines the effective neighbourhood size (expressed in voxels).
13 Consequently, the exponential term represents the distance-dependent attenuation
14 of the saliency. The orientation of the vote, \vec{N} , is obtained by dragging the vector
15 $\vec{v}_1 = [\cos\alpha(\mathbf{T}(\mathbf{x}')), \sin\alpha(\mathbf{T}(\mathbf{x}'))]$ that determines the orientation of the stick ten-
16 sor at voter point \mathbf{x}' , along the arc from \mathbf{x}' to the receiver point \mathbf{x} (Figure 2(A)):
17 $\vec{N} = \mathbf{R}(2\phi)\vec{v}_1$, with $\mathbf{R}()$ denoting the rotation matrix.

18
19
20
21
22
23
24
25
26 Figure 2(B) depicts the stick voting tensor field, which is the collection of
27 the second order votes cast by a voter located at the origin, whose stick tensor
28 has unit saliency and orientation along the x-axis: $\mathbf{V}(\mathbf{x}, 0)$. The extension of this
29 voting kernel is limited by σ_v (in practice it is about $3 \times \sigma_v$) and $\phi \leq 45^\circ$ (Medioni
30 et al., 2000; Tong et al., 2004).
31

32
33
34
35
36 The voting mechanism expressed in Eq. (10) is usually interpreted as fol-
37 lows (Medioni et al., 2000; Tong et al., 2004). To compute the votes cast by a
38 voter \mathbf{x}' , the stick voting field $\mathbf{V}(\mathbf{x}, 0)$ is placed at the location of the voter and
39 with its orientation $\alpha = \alpha(\mathbf{T}(\mathbf{x}'))$ (Medioni et al., 2000; Tong et al., 2004), using
40 tensor rotation operations:
41
42
43
44

$$45 \quad \mathbf{V}(\mathbf{x} - \mathbf{x}', \alpha) = \mathbf{R}(\alpha) \mathbf{V}(\mathbf{R}^{-1}(\alpha)(\mathbf{x} - \mathbf{x}'), 0) \mathbf{R}^{-1}(\alpha) \quad (11)$$

46
47
48
49
50 Figure 2(C) shows a sketch of this transformation and voting process. Most im-
51 plementations of tensor voting are based on this interpretation.
52
53
54
55
56
57
58

1
2
3
4
5
6
7
8
9 *3.1.4. Vote collection and interpretation of results*

10 The votes received at each voxel \mathbf{x} are collected and accumulated by tensor
11 addition so as to yield the resulting output tensor $\mathbf{U}(\mathbf{x})$. Thus, the voting process
12 described above can be considered as a tensor convolution of the input tensor field
13 $\mathbf{T}(\mathbf{x})$ with the voting field $\mathbf{V}(\mathbf{x}, \alpha)$:
14
15
16
17
18
19

$$20 \quad \mathbf{U}(\mathbf{x}) = \sum_{\mathbf{x}' \in \text{Neigh}(\mathbf{x})} S(\mathbf{T}(\mathbf{x}')) \mathbf{V}(\mathbf{x} - \mathbf{x}', \alpha(\mathbf{T}(\mathbf{x}'))) \quad (12)$$

21 where \mathbf{x}' represents a voter within the neighborhood of \mathbf{x} , which has saliency
22 $S(\mathbf{T}(\mathbf{x}'))$ and orientation $\alpha(\mathbf{T}(\mathbf{x}'))$.
23
24
25
26

27 After TV, the output tensor field $\mathbf{U}(\mathbf{x})$ is expected to have more coherent struc-
28 tural information. Voxels belonging to the same geometric feature will have
29 strengthened each other and their tensors will have been modified to enhance the
30 underlying global structure. Interpretation of the final tensors is carried out as de-
31 scribed above, in Section 3.1.1, leading to a more reliable estimates of **curves** (i.e.
32 voxels with high **curve** saliency $\lambda_1 - \lambda_2$, and with the normal to the **curve** pointed
33 by \vec{v}_1).
34
35
36
37
38
39
40

41 *3.2. Efficient implementation of Tensor Voting with steerable filters*

42 Tensor voting is a computationally demanding procedure. The standard imple-
43 mentation consists of pre-computing and storing the voting field $\mathbf{V}(\mathbf{x}, 0)$ (Eq. (10)).
44 Translation and rotation of the voting field throughout the image space needed for
45 casting votes (Eqs. (11; 12)) is done by interpolation. Alternatively, storing all ro-
46 tated voting fields would reduce the voting process to simple look-up operations
47 and interpolation, but the memory consumption would be higher. There exists,
48 however, a more efficient implementation that takes advantage of the theory of
49 steerable filters (Franken et al., 2006). The requirement for selective orientation
50
51
52
53
54
55
56
57
58
59
60
61
62
63
64
65

of the voting field is similar to that encountered with scalar oriented filters, the optimal implementation of which is carried in the framework of the theory of steerable filters (Freeman and Adelson, 1991).

In image processing, a steerable filter is a filter that can be oriented in an arbitrary direction just by a linear combination of a finite number of predefined rotations of the filter (so-called basis functions or filters) (Freeman and Adelson, 1991). Rotation of the steerable filter h by an angle α can be shown as:

$$h(\mathbf{x}, \alpha) = \sum_{m=1}^M k_m(\alpha) h_m(\mathbf{x}) \quad (13)$$

where $h_m(\mathbf{x})$ are the basis filters, $k_m(\alpha)$ are the linear coefficients that depend on the rotation angle α , m denotes the index of the basis filters and the number of basis filters is M . In practice, in order to reduce the number of the basis filters required to steer the filter, they are taken from the nonzero coefficients of the angular Fourier decomposition of the filter (Freeman and Adelson, 1991). Filtering an image $f(\mathbf{x})$ with the oriented filter $h(\mathbf{x}, \alpha)$ then becomes:

$$f(\mathbf{x}) * h(\mathbf{x}, \alpha) = \sum_{m=1}^M k_m(\alpha) (f(\mathbf{x}) * h_m(\mathbf{x})) \quad (14)$$

where $*$ denotes convolution. In other words, an image filtered at an arbitrary direction can be computed by a simple linear combination of the image filtered with M basis filters h_m , with coefficients $k_m(\alpha)$. If M is sufficiently small, this turns out to be a very efficient method for arbitrary oriented filtering of images.

Here we briefly describe the two key aspects of the derivation of steerable approach to 2D TV in order to understand the internals of our implementation. This derivation, together with the mathematical details, were nicely presented in (Franken et al., 2006). First, steerable tensor voting uses a saliency decay function different from the original one (exponential term in Eq. (10)) so as to make

the voting field bandlimited (i.e. to have a finite number of nonzero coefficients of the angular Fourier decomposition): $\frac{1}{16}e^{\frac{-r^2}{2\sigma_v^2}} \cos^4 \phi$.

Second, as explained in Section 3.1.1, the tensors used in 2D TV are 2×2 symmetric matrices having three independent components: $\{t_{xx}, t_{xy}, t_{yy}\}$. Tensor rotation (Eq. (11)) can be computed using a similarity transformation (Golub and van Loan, 1996), as thoroughly described in (Franken et al., 2006) for a general case. Furthermore, rotation of a pure stick tensor, as required here for votes, simplifies to the rotation of a single function V_{-2} derived from the components of the tensor (Franken et al., 2006): $V_{-2} = t_{xx} + 2it_{xy} - t_{yy}$. This function allows easy calculation of the saliency and orientation of the tensor, as defined in Eqs. (7) and (8): $S(\mathbf{V}) = |V_{-2}|$ and $\alpha(\mathbf{V}) = \frac{1}{2} \arg(V_{-2})$, respectively.

Thus, the steerable tensor field rotated by an angle α is finally reduced to the rotation of the steerable function V_{-2} (Franken et al., 2006):

$$V_{-2}(\mathbf{x}, \alpha) = \sum_{m=0}^4 k_m(\alpha) V_m(\mathbf{x}) \quad (15)$$

where k_m are the linear coefficients:

$$k_m(\alpha) = e^{-2i(m-1)\alpha} \quad (16)$$

and $V_m(\mathbf{x})$ are the basis filters given by:

$$V_m(\mathbf{x}) = \gamma_m e^{-\frac{x^2+y^2}{2\sigma_v^2}} \left(\frac{x+iy}{\sqrt{x^2+y^2}} \right)^{2m}, \text{ for } \mathbf{x} = (x, y) \neq (0, 0) \quad (17)$$

where γ_m has constant values: $\{1, 4, 6, 4, 1\}$ for $m = 0 \dots 4$, respectively.

Therefore, the voting process originally expressed as a tensor convolution (Eq. (12)) is reduced to a scalar steerable convolution that, similarly to Eq. (14),

can be expressed as:

$$U_{-2}(\mathbf{x}) = S(\mathbf{T}(\mathbf{x})) * V_{-2}(\mathbf{x}, \alpha(\mathbf{T}(\mathbf{x}))) = \sum_{m=0}^4 k_m(\alpha(\mathbf{T}(\mathbf{x}))) (S(\mathbf{T}(\mathbf{x})) * V_m(\mathbf{x})) \quad (18)$$

From here, calculation of the output saliency and orientation is straightforward, as mentioned above:

$$\begin{aligned} S(\mathbf{U}(\mathbf{x})) &= |U_{-2}(\mathbf{x})| \\ \alpha(\mathbf{U}(\mathbf{x})) &= \frac{1}{2} \arg(U_{-2}(\mathbf{x})). \end{aligned} \quad (19)$$

Eqs. (18) and (19) reveal that only five convolutions are required to accomplish TV. Moreover, computation of these convolutions in Fourier speeds up the calculation significantly (Franken et al., 2006). Therefore, this steerable approach provides a very efficient implementation of TV, well suited to deal with large tomograms commonly encountered in ET.

The implementation of steerable 2D TV can then be summarised as follows:

- **Initialization of the input tensor field.**

The saliency and orientation of the input tensor field, ($S_{\text{in}}(\mathbf{x})$ and $\alpha_{\text{in}}(\mathbf{x})$) are initialized based on the eigenvalues (λ_i) and eigenvectors (\vec{v}_i) of the 2D Hessian or Structure tensor of the input 2D slice (see Eqs. (7) and (8)):

$$S_{\text{in}}(\mathbf{x}) = S(\mathbf{T}(\mathbf{x})) = |\lambda_1 - \lambda_2| \quad (20)$$

$$\alpha_{\text{in}}(\mathbf{x}) = \alpha(\mathbf{T}(\mathbf{x})) = \arccos(\vec{v}_1 \cdot \hat{e}_x) \quad (21)$$

- **Tensor voting.**

1
2
3
4
5
6
7
8
9 The output saliency $S_{\text{out}}(\mathbf{x})$ is computed according to the following expres-
10 sion derived from Eqs. (18) and (19):
11
12

$$13 S_{\text{out}}(\mathbf{x}) = S(\mathbf{U}(\mathbf{x})) = \left| \sum_{m=0}^4 k_m(\alpha_{\text{in}}(\mathbf{x})) (S_{\text{in}}(\mathbf{x}) * V_m(\mathbf{x})) \right| \quad (22)$$

14
15
16
17
18 with $k_m(\alpha_{\text{in}}(\mathbf{x}))$ and $V_m(\mathbf{x})$ given by Eqs. (16) and (17), respectively, and the
19 convolutions being computed in Fourier space.
20
21
22

23 As mentioned above, our approach to apply TV on a tomogram involves appli-
24 cation of this efficient 2D computational procedure to 2D slices of the tomogram
25 along the three major axes. The final output surface saliency for each voxel is
26 taken as the average of the three curve saliency values available. To reduce the
27 distortion caused by the missing wedge, the input saliency values of the voxels
28 with orientation $|\alpha(\mathbf{T}(\mathbf{x}))| > \omega$ are set to zero, with ω being the maximum tilt an-
29 gle used in the tilt-series acquisition. This constraint is applied for voxels in xz-
30 and yz-planes.
31
32
33
34
35
36
37

38 Figure 3 shows the ability of TV to detect membranes correctly even in the
39 presence of membrane-attached structures and to fill the gaps present in mem-
40 branes when applied to a cellular cryo-tomogram. Supplementary Figure S1 also
41 illustrates that the output saliency proves to be well suited for automated mem-
42 brane detection.
43
44
45
46
47
48
49
50
51
52
53
54
55
56
57
58
59
60
61
62
63
64
65

4. Tensor Voting-based membrane detection

In this section we present the whole procedure devised to detect membranes. It relies on an improved local detector of membranes (or plane-like structures in general) based on TV. The use of TV provides robustness so that at the end of the process membranes are extracted by a simple thresholding operation. This procedure is named TomoSegMemTV and consists of the following stages:

1. *Filtering and scale-space of the input tomogram.*

This stage aims to reduce noise and filter out structural information smaller than the scale of interest σ . It also helps to ensure that edges and ridges approach Gaussian profiles, which is important for Stage 3. Usually a Gaussian low-pass filtering is used, but more aggressive noise reduction techniques, such as the anisotropic nonlinear diffusion filter (Frangakis and Hegerl, 2001; Fernandez and Li, 2003, 2005) might be used before scale-space so as to substantially remove noise, flatten background and preserve and enhance features of interest. However, to our experience, the actual effect that this filtering has on the performance of the segmentation algorithm is not significant.

2. *Tensor voting on surface saliency.*

TV is applied to enhance the local surface information provided by the Hessian or the Structure tensor of the scale-spaced tomogram. If the aim is to detect ridges, the Hessian tensor is used as an input to TV. If edges are to be detected, the Structure tensor is used. Note that in the latter case the output surface information will refer to the middle of the edges but it would be otherwise equivalent to the information obtained by the use of the Hessian tensor, as explained in Section 2.2. Hence, the remaining stages proceed in

the same way, regardless of the input tensor used. The performance of TV applied to a cryo-tomogram of a synapse is illustrated in Figure 4.

3. Local surface detection and characterization.

The NMS detector defined in Eq. (3) is employed to detect membrane structures from the surface saliency obtained by the previous stage. This results in a 1-voxel-thick surface, which represents the centerlines of the potential membranes (Figure 5(E)). Next, the extracted points are subjected to characterization through planarity descriptors, which determine the probability of belonging to a surface. As it was done for vessel detection in MRI (Frangi et al., 1998) and cell membranes in optical microscopy (Mosaliganti et al., 2012), 3D planarity map is defined by the following mathematical expression:

$$P(\mathbf{x}) = \begin{cases} P_s(\mathbf{x}) \cdot P_p(\mathbf{x}), & \forall \mathbf{x} \in \mathcal{S} \\ 0, & \text{otherwise} \end{cases} \quad (23)$$

with

$$P_s(\mathbf{x}) = 1 - e^{-\lambda_1(\mathbf{x})/\hat{\lambda}_1} \quad P_p(\mathbf{x}) = 1 - e^{-p(\mathbf{x})/\hat{p}}, \quad (24)$$

where \mathbf{x} are voxel coordinates, \mathcal{S} is a binary mask resulting from the NMS operation, and $\hat{\cdot}$ is the arithmetic mean of the samples in the \mathcal{S} domain. p is the descriptor that measures planarity of a structure according to the eigenvalues of the Hessian tensor of the scale-spaced volume:

$$p = 1 - \frac{|\lambda_2|}{|\lambda_1|}, \quad (25)$$

P_s enhances points that stand out from the background, whereas P_p those exhibiting locally planar structure. These definitions ensure that the planarity map takes values in the range $[0, 1]$ and that the contribution of factors P_s and P_p to P are equally important. The weight of the factors λ_1

1
2
3
4
5
6
7
8
9 and $p(x)$ is automatically controlled through their means in \mathcal{S} . The example
10 presented in Figure 5 shows that these descriptors complement each other.
11
12

13 4. *Tensor voting for bridging gaps.*
14

15 It is possible to observe in Figure 5 that the descriptor P gives an output that
16 is similar to the expected segmentation. However, direct thresholding of P
17 may still produce holes in those membrane regions with lower P values. In
18 order to make P more uniform and fill potential gaps, TV is applied on the
19 Hessian tensor of P , using the same parameter configuration as in Stage 2.
20 Prior to TV, P is subjected to Gaussian filtering ($\sigma \approx 0.5$) to make it slightly
21 denser (note that P is sparse as it results from a NMS operation).
22
23
24
25
26
27

28 5. *Local membrane detector.*
29

30 The map resulting from the previous stage could already be used as a local
31 detector of membranes. However, we find it useful to proceed with the
32 eigen-analysis of the Hessian tensor of that map to extract the absolute value
33 of the largest eigenvalue ($|\lambda_1|$, with $\lambda_1 < 0$; 0 otherwise), followed by NMS.
34 The resulting map (Figure 6(Left)) is more robust than P (Figure 5(D)) in
35 the sense that the difference between the membranes and the other points
36 is higher. This is because $|\lambda_1|$ is more sensitive to the density and can thus
37 detect true membrane points. In addition, the eigen-analysis performed at
38 this stage provides the information about the direction perpendicular to the
39 membrane (\vec{v}_1) at all membrane points.
40
41
42
43
44
45
46
47
48

49 6. *Thresholding and global analysis.*
50

51 This post-processing stage aims to analyze and integrate, at a global scale,
52 the local structural information derived in the previous stages. First, spuri-
53 ous structures have to be rejected. The robustness of the membrane detector
54
55
56
57
58
59
60
61
62
63
64
65

1
2
3
4
5
6
7
8
9 of the previous stage enables this rejection by a simple standard threshold-
10 ing procedure (Figure 6(Center)). Second, a global analysis, based for in-
11 stance on volumetric size, helps to discern whether the segmented structures
12 are actual membranes and also to distinguish between different types of
13 membranes, as described previously (Martinez-Sanchez et al., 2011) (Fig-
14 ure 6(Right)). More sophisticated global analysis could be used, such as
15 that based on clustering of the local membrane density profile (along the di-
16 rection perpendicular to the membrane \vec{v}_1) (Martinez-Sanchez et al., 2013).
17
18
19
20
21
22
23
24

25 The output of TomoSegMemTV consists of 1-voxel thick surfaces. The mem-
26 brane thickness can be easily increased by means of morphological operations.
27

28
29 The whole procedure works in 3D except Stages 2 and 4, which are based on
30 the application of TV to 2D slices, as described earlier. Stages 3 and 5, however,
31 are based on the 3D Hessian tensor (see Section 2) calculated for all voxels of the
32 corresponding input map.
33
34
35
36

37 The tuning of the parameters required by the algorithm is relatively simple.
38 The key parameter for TV is σ_v , which is related to the SNR/contrast. The poorer
39 SNR/contrast conditions are, the higher σ_v should be. As this parameter defines
40 the neighbourhood in TV, higher values tend to emphasize larger membranes over
41 smaller ones (for instance, compare synaptic membranes to vesicles in Figure 4).
42 In our experiments, values in the range from 5 to 15 voxels were taken. The
43 threshold t_b on the response of the membrane detector is required at the last stage
44 to produce the output binary map. It can be easily set by the user based on visual
45 inspection (see Figure 6). At this point, a threshold on the volumetric size t_v
46 of the segmented structures may be required to extract the targeted membranes.
47 The scale σ for scale-space operation should be tuned according to the membrane
48
49
50
51
52
53
54
55
56
57
58

1
2
3
4
5
6
7
8
9 thickness in the tomograms. The parameter ω is given by the maximum tilt angle
10 used in the tilt-series acquisition. With regard to the parameters δ and t_M of the
11 NMS detector (Eq. (3)), in this work they were fixed to 0.71 and 0.03, respectively.
12
13
14

15 **5. Results**

16 *5.1. Validation of the method*

17
18
19
20 A quantitative analysis based on a synthetic phantom tomogram under differ-
21 ent noise conditions was performed to validate TomoSegMemTV. The evaluation
22 includes a comparison with a standard technique, template matching.
23
24

25
26 Template matching underlies recent approaches for automated segmentation
27 of specific structures (Fernandez, 2012), including membranes (Lebbink et al.,
28 2007, 2010). In these works, a template suitable for membranes (typically a
29 cuboid shape) is rotated, adjusted to account for the distortion caused by the miss-
30 ing wedge and cross-correlated with the tomogram (Lebbink et al., 2007). The
31 resulting cross-correlation map, which gathers the results from all possible rotated
32 versions of the template, is then thresholded to obtain the final segmentation.
33
34
35
36
37
38

39 The phantom (ground truth) that we have designed for this validation in-
40 cludes a number of geometric features resembling membranes, vesicles and tubu-
41 lar structures (see Supplementary Figures S3 and S4). To simulate macromolec-
42 ular crowding, the *Saccharomyces cerevisiae* 80S ribosome structure, taken from
43 the EM databank (<http://emdatbank.org>; entry emd-1076), was properly scaled,
44 randomly oriented and placed throughout the phantom tomogram. We tested dif-
45 ferent number of ribosomes (1000, 5000 and 10000) and different noise conditions
46 (SNR=0.05, 0.1 and 2). For template matching, we used the Molmatch implemen-
47 tation (Forster et al., 2010) with a template consisting of a plane with the thickness
48 of the membranes in the phantom. For TomoSegMemTV, σ and σ_v were set to
49
50
51
52
53
54
55
56
57
58

1
2
3
4
5
6
7
8
9 1 and 10, respectively. In order to ensure a fair comparison between template
10 matching and TomoSegMemTV, the same strategy was used for the thresholding
11 and global analysis (see Supplementary Material, Section S.5.1).
12
13

14
15 The metrics used for the quantitative analysis are the following. First, the frac-
16 tion of true positives (TPF; also known as sensitivity) is the fraction of membrane
17 points that have been correctly classified. Second, the fraction of true negatives
18 (TNF; also known as specificity) is the fraction of non-membrane points that have
19 been correctly left out of the membranes. Third, the precision (PR) gives the pro-
20 portion of overlapping/concordance between the phantom and the segmentation
21 (see (Garduno et al., 2008; Martinez-Sanchez et al., 2011, 2013) for more infor-
22 mation about these metrics). If H_g and H are the binary representations of the
23 ground truth (i.e. the phantom) and the segmentation result respectively, these
24 metrics are defined as: $TPF = \frac{|H \cap H_g|}{|H_g|}$, $TNF = \frac{|H^C \cap H_g^C|}{|H_g^C|}$, and $PR = \frac{|H \cap H_g|}{|H \cup H_g|}$, where $|\cdot|$ is
25 the number of elements in a set, \cup and \cap represent the union and intersection set
26 operations, respectively, and A^C denotes the complement of set A .
27
28
29
30
31
32
33
34
35
36
37

38 Tables 1 and 2 summarize the results obtained from the evaluation. As ex-
39 pected, the performance of both techniques deteriorates with decreasing SNR and
40 increasing macromolecular crowding. In particular, the latter factor severely de-
41 grades the performance of template matching. These results show that TomoSeg-
42 MemTV is much more robust to noise and crowding and outperforms template
43 matching, having sensitivity (TPF) around 90%. It is remarkable that TomoSeg-
44 MemTV under the worst conditions (SNR=0.05 and 10000 ribosomes) presents
45 behaviour similar to template matching in the best scenario tested here (SNR=2
46 and 1000 ribosomes). Supplementary Figures S3 and S4 show examples of the
47 performance of the methods on the phantom.
48
49
50
51
52
53
54
55
56
57
58
59
60
61
62
63
64
65

1
2
3
4
5
6
7
8
9 Similar behaviour is observed when applied to experimental cryo-tomograms,
10 as presented in Supplementary Section S.5.1 and Figure S5. There, an example of
11 cryo-tomogram of neuronal synapse shows the limitations of template matching.
12 No optimal threshold is found, leading to false positives and negatives. On the
13 contrary, the thresholding in TomoSegMemTV is straightforward and membranes
14 turn out to be well delineated.
15
16
17
18
19
20

21 *5.2. Applications to experimental datasets*

22
23 In this section, illustrative examples of the application of TomoSegMemTV to
24 several experimental datasets are shown.
25
26

27 *5.2.1. Human Immunodeficiency virus*

28
29 The segmentation method presented here was applied to a cryo-tomogram of
30 HIV-1 virions that was taken from the EM databank (<http://emdatbank.org>; entry
31 emd-1155) (Briggs et al., 2006). This tomogram has been often used in the field
32 to test denoising and segmentation algorithms (e.g. (van der Heide et al., 2007;
33 Fernandez, 2009)). The tomogram was first subjected to the membrane detec-
34 tion algorithm that we developed previously, TomoSegMem (Martinez-Sanchez
35 et al., 2011). In general, it allowed good delineation of the outer membranes of
36 the virions, as shown in Figure 7. However, the limitations of the technique are
37 evidenced by some imperfections, such as gaps in the membranes (green arrow-
38 heads) or residual structures apposed to them (yellow arrowheads) that arise from
39 the dense material in the interior of the virions.
40
41
42
43
44
45
46
47
48
49

50 The use of TomoSegMemTV overcame those limitations. Tensor voting and
51 the planarity characterization make the method more robust and more sensitive
52 to membranes, as shown in Figure 7. This is reflected in the continuity of the
53 membranes of the virions, which are free of gaps and spurious protrusions.
54
55
56
57
58

5.2.2. *Caulobacter Crescentus*

As an example of detection of a membrane with edge-like profile, we took a tomogram of *Caulobacter Crescentus*, a gram-negative bacterium, from the Cell-Centered database (<http://ccdb.ucsd.edu>; entry 3647). We focused on the detection of the outer interface of the bacterial wall. To do so, we followed the TomoSegMemTV algorithm but, as already described, we used the Structure tensor at Stage 2 of the algorithm instead of the Hessian tensor (see Section 2). The remaining stages of the algorithm proceeded in the same way as if the Hessian tensor was used. Figure 8 shows that TomoSegMemTV succeeded in detecting the outer membrane.

The availability of information about the normal to the membrane for all segmented points opened up the possibility of further analysis. In this particular case, we extracted density profiles in the direction perpendicular to the membrane to obtain an average density profile at a higher resolution. Supplementary Figure S6 shows the average computed from 31400 orientationally aligned profiles that were calculated from the tomogram of *Caulobacter Crescentus*, using TomoSegMemTV. This figure shows peaks corresponding to the inner membrane, the peptidoglycan layer and the outer interface of the bacterial wall.

5.2.3. *Neuronal synapses*

During the course of this work, TomoSegMemTV has been tested on numerous cryo-tomograms of neuronal synapses. Actually, the developments have been motivated in part by the particular characteristics of those datasets (multiple structures attached to the membranes and/or gaps due to the low SNR and contrast, among other factors), which make automated segmentation especially challenging. Such datasets were used to illustrate the methods presented here. Details

1
2
3
4
5
6
7
8
9 regarding sample preparation and tomogram generation of these datasets can be
10 found in Supplementary Material, Section S.5.2.3.

11
12
13 Synapses consist of pre- and postsynaptic terminals and contain a number
14 of structural components that have to be segmented from the tomograms. The
15 plasma membranes of the interacting neurons (referred to as pre-synaptic and
16 post-synaptic membranes) were detected by the procedure presented here (Fig-
17 ures 6 and 9). At the synapse, those membranes are directly apposed to each
18 other and are separated by a uniform distance, thus defining the synaptic cleft.
19 Output normals provided by TomoSegMemTV allowed the determination of the
20 shortest distance between two membranes at every point. Synaptic membranes
21 were detected based on their high volumetric size. Their portions that delineate
22 the synaptic cleft were labelled based on the distinctive inter-membrane distance
23 (Figure 9). The presynaptic terminal contains machinery for the neurotransmit-
24 ter release and comprises vesicles, as well as short filaments that interconnects
25 the vesicles and tether them to the synaptic membrane. The entire presynaptic
26 cytoplasm was segmented using morphological dilation operations, starting from
27 a point selected by the user and using the segmented membranes as boundaries
28 (Figure 9). Because synaptic vesicles are spherical and have uniform size, they
29 were detected by standard template matching procedures, but taking into account
30 the distortion induced by the missing wedge (Bohm et al., 2000). Figure 10 shows
31 3D views of the segmentations of some datasets.

32 33 34 35 36 37 38 39 40 41 42 43 44 45 46 47 48 49 50 **6. Discussion and Conclusion**

51
52
53 Segmentation of electron tomograms recorded from biological samples is im-
54 portant for the interpretation and visualization of their structural components and
55
56
57
58
59
60
61
62
63
64
65

1
2
3
4
5
6
7
8
9 is necessary for their further computational analysis. Here we present TomoSeg-
10 MemTV, a procedure for membrane segmentation based on Tensor Voting. It
11 relies on an improved local membrane detector that propagates differential infor-
12 mation within the neighbourhood of each voxel in an anisotropic way, according
13 to the underlying global structure. This strategy provides the algorithm with the
14 ability to fill gaps present along the membranes. Moreover, it confers robustness
15 against other structures attached to membranes and against the low SNR typi-
16 cally found in cryo-tomograms. The algorithm has been validated and tested on
17 a number of experimental datasets, with special focus on the segmentation of the
18 structures required for the analysis of neuronal synapses.
19
20
21
22
23
24
25
26
27

28 TomoSegMemTV can detect structures with either ridge or edge profiles, by
29 simply choosing the Hessian tensor or the Structure Tensor based local detec-
30 tor, respectively. Moreover, the algorithm yields not only the set of segmented
31 membrane points, but also the normals to the membranes. **This enables more**
32 **sophisticated structural analyses, such as characterization and classification of**
33 **membranes according to their local properties (Martinez-Sanchez et al., 2013).**
34 TomoSegMemTV can also be used for determination of average membrane pro-
35 files, enabling automated tomographic data analysis. Previous approaches only
36 allowed limited averaging, used semi-automated procedures or required sophis-
37 ticated techniques (Li et al., 2007; Hoffmann et al., 2008; Zuber et al., 2008;
38 Tocheva et al., 2011).
39
40
41
42
43
44
45
46
47
48

49 The output yielded by the local detector of TomoSegMemTV turned out to be
50 very robust, which enabled the use of a simple thresholding procedure to select
51 the putative true membrane points. Therefore, this constitutes an advantage over
52 other methods used in the field including our previous detector (Martinez-Sanchez
53
54
55
56
57
58
59
60
61
62
63
64
65

1
2
3
4
5
6
7
8
9 et al., 2011), where a more complex hysteresis thresholding stage was required.
10 Moreover, template matching is a prominent technique that supports segmenta-
11 tion approaches targeting filamentous or membranous structures (Lebbink et al.,
12 2007; Rigort et al., 2012). However, template matching tends to produce spuri-
13 ous correlation peaks in overcrowded environments, particularly under low SNR
14 as is the case in electron cryo-tomography, which limits the performance of the
15 thresholding operation over the cross-correlation map. As a consequence, an op-
16 timum threshold cannot be found and the thresholded map often contains residual
17 false positives or gaps in the targeted structures (false negatives). By contrast,
18 the robustness of TomoSegMemTV makes it less susceptible to this problem. An
19 additional advantage over template matching is that methods based on differential
20 geometry are more flexible to adapt to high membrane curvature (Lebbink et al.,
21 2007).

22
23
24
25
26
27
28
29
30
31
32
33
34 A quantitative evaluation of phantom datasets has been performed using stan-
35 dard quality metrics for the task of membrane detection under realistic noise and
36 crowding conditions. This analysis has confirmed that the algorithm performs
37 well under different noise levels, including very low SNR, and in the presence
38 of a large macromolecular population. Moreover, this assessment has shown that
39 TomoSegMemTV clearly outperforms template matching. These objective re-
40 sults have also been reflected on the application to experimental datasets, where
41 TomoSegMemTV exhibited very good behaviour under different conditions.

42
43
44
45
46
47
48
49 An important benefit from the user’s point of view concerns parameter setting.
50 Compared to our previous method (Martinez-Sanchez et al., 2011), the number of
51 key parameters is reduced. Some of them are fixed by the experimental imaging
52 conditions, while the tuning of others is straightforward. Essentially, only the
53
54
55
56
57
58

1
2
3
4
5
6
7
8
9 following parameters need to be tuned: the scale of Tensor Voting σ_v , which
10 depends on the SNR and the membrane size, the threshold applied to the local
11 membrane detector and the volume threshold used in the global analysis stage,
12 which is determined by the size of membranes.
13
14

15
16 The implementation of TomoSegMemTV follows a steerable approach to ten-
17 sor voting, which makes it particularly efficient to deal with the large datasets
18 commonly found in electron tomography. In addition, we have applied multi-
19 threading techniques to further accelerate the program (Fernandez, 2008). As a
20 result, tomograms of typical size are segmented in a matter of minutes on stan-
21 dard multicore computers. This is an advantage over template matching, which
22 requires significant processing time (Bohm et al., 2000; Lebbink et al., 2007). A
23 software package implementing TomoSegMemTV has been developed for public
24 use and it is available upon request. The software has been developed in Matlab[®],
25 though computational demanding routines were coded in C++ in order to increase
26 the execution speed. A complementary package, SynapSegTools, with Graphical
27 User Interface for intuitive and friendly segmentation of synapsis is also available.
28
29

30 The segmentation procedure presented here may facilitate subsequent higher
31 resolution structural studies. For example, the precise membrane localization
32 and orientation can provide alignment for subtomogram averaging of membrane-
33 associated complexes (e.g. (Pfeffer et al., 2012; Zanetti et al., 2013)). Moreover,
34 our future interests also include further development of the tensor voting algo-
35 rithm to detect other structures, such as curvilinear components or macromolecu-
36 lar complexes.
37
38
39
40
41
42
43
44
45
46
47
48
49
50
51
52
53
54
55
56
57
58
59
60
61
62
63
64
65

1
2
3
4
5
6
7
8
9
10
11
12
13
14
15
16
17
18
19
20
21
22
23
24
25
26
27
28
29
30
31
32
33
34
35
36
37
38
39
40
41
42
43
44
45
46
47
48
49
50
51
52
53
54
55
56
57
58
59
60
61
62
63
64
65

Acknowledgements

The authors are very grateful to Prof. W. Baumeister for hosting A.M.-S. (Jul-Dec 2012) and giving him the opportunity to interact with the scientists at the Max-Planck Institute for Biochemistry as well as giving him access to its infrastructures. The authors also wish to thank Nikolas Schrod for discussions and useful feedback. This work has been partially supported by the Spanish MICINN and MINECO (TIN2008-01117, TIN2012-37483, EEBB-I-12-04696), J. Andalu- cia (P10-TIC-6002, P11-TIC-7176), in part thanks to European Reg. Dev. Funds (ERDF). AMS was a fellow of the Spanish FPI programme.

1
2
3
4
5
6
7
8
9 **References**

- 10
11 Bohm, J., Frangakis, A. S., Hegerl, R., Nickell, S., Typke, D., Baumeister, W.,
12 2000. Toward detecting and identifying macromolecules in a cellular context:
13 Template matching applied to electron tomograms. *Proc. Natl. Acad. Sci. USA*
14 97, 14245–14250.
15
16
17
18
19
20 Briggs, J. A., Grunewald, K., Glass, B., Forster, F., Krausslich, H.-G., Fuller,
21 S. D., 2006. The mechanism of HIV-1 core assembly: insights from three-
22 dimensional reconstructions of authentic virions. *Structure* 14, 15–20.
23
24
25
26
27 Cyrklaff, M., Risco, C., Fernandez, J. J., Jimenez, M. V., Esteban, M., Baumeister,
28 W., Carrascosa, J. L., 2005. Cryo-electron tomography of vaccinia virus. *Proc.*
29 *Natl. Acad. Sci. USA* 102, 2772–2777.
30
31
32
33
34 Fernandez, J. J., 2008. High performance computing in structural determination
35 by electron cryomicroscopy. *J. Struct. Biol.* 164, 1–6.
36
37
38
39 Fernandez, J. J., 2009. Tomobflow: feature-preserving noise filtering for electron
40 tomography. *BMC Bioinformatics* 10:178.
41
42
43
44 Fernandez, J. J., 2012. Computational methods for electron tomography. *Micron*
45 43, 1010–1030.
46
47
48
49 Fernandez, J. J., Li, S., 2003. An improved algorithm for anisotropic nonlinear
50 diffusion for denoising cryo-tomograms. *J. Struct. Biol.* 144, 152–161.
51
52
53
54
55
56
57
58
59
60
61
62
63
64
65

- 1
2
3
4
5
6
7
8
9 Forster, F., Han, B. G., Beck, M., 2010. Visual proteomics. *Methods Enzymol.*
10 483, 215–243.
11
12
13 Frangakis, A. S., Hegerl, R., 2001. Noise reduction in electron tomographic recon-
14 structions using nonlinear anisotropic diffusion. *J. Struct. Biol.* 135, 239–250.
15
16
17 Frangi, A. F., Niessen, W. J., Vincken, K. L., Viergever, M. A., 1998. Multiscale
18 vessel enhancement filtering. In: *Medical Image Computing and Computer-*
19 *Assisted Intervention—MICCAI’98*. Vol. 1496 of *Lecture Notes in Computer*
20 *Science*. Springer, pp. 130–137.
21
22
23
24
25
26 Franken, E., van Almsick, M., Rongen, P., Florack, L., ter Haar Romeny, B., 2006.
27 An efficient method for tensor voting using steerable filters. In: *Computer Vi-*
28 *sion – ECCV 2006*. Vol. 3954 of *Lecture Notes in Computer Science*. Springer,
29 pp. 228–240.
30
31
32
33
34
35 Freeman, W. T., Adelson, E. H., 1991. The design and use of steerable filters.
36 *IEEE Trans. Pattern Anal. Mach. Intell.* 13, 891–906.
37
38
39 Garduno, E., Wong-Barnum, M., Volkman, N., Ellisman, M. H., 2008. Segmen-
40 tation of electron tomographic data sets using fuzzy set theory principles. *J.*
41 *Struct. Biol.* 162, 368–379.
42
43
44
45
46 Golub, G., van Loan, C., 1996. *Matrix Computations*. The Johns Hopkins Univer-
47 sity Press, London, UK.
48
49
50 Hoffmann, C., Leis, A., Niederweis, M., Plitzko, J. M., Engelhardt, H., 2008.
51 Disclosure of the mycobacterial outer membrane: cryo-electron tomography
52 and vitreous sections reveal the lipid bilayer structure. *Proc. Natl. Acad. Sci.*
53 *USA* 105, 3963–3967.
54
55
56
57
58

- 1
2
3
4
5
6
7
8
9 Lebbink, M. N., Geerts, W. J., van der Krift, T. P., Bouwhuis, M., Hertzberger,
10 L. O., Verkleij, A. J., Koster, A. J., 2007. Template matching as a tool for
11 annotation of tomograms of stained biological structures. *J. Struct. Biol.* 158,
12 327–335.
13
14
15
16
17 Lebbink, M. N., Jimenez, N., Vocking, K., Hekking, L. H., Verkleij, A. J., Post,
18 J. A., 2010. Spiral coating of the endothelial caveolar membranes as revealed
19 by electron tomography and template matching. *Traffic* 11, 138–150.
20
21
22
23
24 Li, Z., Trimble, M. J., Brun, Y. V., Jensen, G. J., 2007. The structure of FtsZ
25 filaments in vivo suggests a force-generating role in cell division. *EMBO J.* 26,
26 4694–4708.
27
28
29
30
31 Lucic, V., Rigort, A., Baumeister, W., 2013. Cryo-electron tomography: the chal-
32 lenge of doing structural biology in situ. *J. Cell Biol.* 202, 407–419.
33
34
35
36 Martinez-Sanchez, A., Garcia, I., Fernandez, J. J., 2011. A differential structure
37 approach to membrane segmentation in electron tomography. *J. Struct. Biol.*
38 175, 372–383.
39
40
41
42 Martinez-Sanchez, A., Garcia, I., Fernandez, J. J., 2013. A ridge-based framework
43 for segmentation of 3D electron microscopy datasets. *J. Struct. Biol.* 181, 61–
44 70.
45
46
47
48
49 Medioni, G., Lee, M. S., Tang, C. K., 2000. A computational framework for seg-
50 mentation and grouping. Elsevier Science, Amsterdam, The Netherlands.
51
52
53
54 Mosaliganti, K. R., Noche, R. R., Xiong, F., Swinburne, I. A., Megason,
55 S. G., 2012. ACME: automated cell morphology extractor for comprehen-
56
57
58
59
60
61
62
63
64
65

1
2
3
4
5
6
7
8
9 sive reconstruction of cell membranes. PLoS Comput. Biol. 8, e1002780. doi:
10
11 10.1371/journal.pcbi.1002780.
12

13 Moussavi, F., Heitz, G., Amat, F., Comolli, L. R., Koller, D., Horowitz, M., 2010.
14 3D segmentation of cell boundaries from whole cell cryogenic electron tomog-
15 16 3D segmentation of cell boundaries from whole cell cryogenic electron tomog-
17 18 19 raphy volumes. J. Struct. Biol. 170, 134–145.

20 Nurgaliev, D., Gatanov, T., Needleman, D. J., 2010. Automated identification of
21 22 23 microtubules in cellular electron tomography. Methods Cell Biol. 97, 475–495.
24

25 Pfeffer, S., Brandt, F., Hrabe, T., Lang, S., Eibauer, M., Zimmermann, R., Forster,
26 27 28 F., 2012. Structure and 3D arrangement of endoplasmic reticulum membrane-
29 30 associated ribosomes. Structure 20, 1508–1518.

31 Rigort, A., Günther, D., Hegerl, R., Baum, D., Weber, B., Prohaska, S., Medalia,
32 33 34 O., Baumeister, W., Hege, H.-C., 2012. Automated segmentation of electron
35 36 37 tomograms for a quantitative description of actin filament networks. J. Struct.
38 39 Biol. 177, 135–144.

40 Sandberg, K., Brega, M., 2007. Segmentation of thin structures in electron micro-
41 42 43 graphs using orientation fields. J. Struct. Biol. 157, 403–415.
44

45 Tocheva, E. I., Matson, E. G., Morris, D. M., Moussavi, F., Leadbetter, J. R.,
46 47 48 Jensen, G. J., 2011. Peptidoglycan remodeling and conversion of an inner mem-
49 50 brane into an outer membrane during sporulation. Cell 146, 799–812.

51 Tong, W. S., Tang, C. K., Mordohai, P., Medioni, G., 2004. First order augmen-
52 53 54 tation to tensor voting for boundary inference and multiscale analysis in 3D.
55 56 IEEE Trans. Pattern Anal. Mach. Intell. 26, 594–611.
57

- 1
2
3
4
5
6
7
8
9 van der Heide, P., Xu, X. P., Marsh, B. J., Hanein, D., Volkman, N., 2007. Efficient automatic noise reduction of electron tomographic reconstructions based on iterative median filtering. *J. Struct. Biol.* 158, 196–204.
10
11
12
13
14
15
16 Volkman, N., 2002. A novel three-dimensional variant of the Watershed transform for segmentation of electron density maps. *J. Struct. Biol.* 138, 123–129.
17
18
19
20 Volkman, N., 2010. Methods for segmentation and interpretation of electron tomographic reconstructions. *Methods Enzymol.* 483, 31–46.
21
22
23
24
25 Weber, B., Greenan, G., Prohaska, S., Baum, D., Hege, H. C., Muller-Reichert, T., Hyman, A. A., Verbavatz, J. M., 2012. Automated tracing of microtubules in electron tomograms of plastic embedded samples of *Caenorhabditis elegans* embryos. *J. Struct. Biol.* 178, 129–138.
26
27
28
29
30
31
32
33
34 Weickert, J., 1998. *Anisotropic Diffusion in Image Processing*. Teubner-Verlag, Stuttgart, Germany.
35
36
37
38 Zanetti, G., Prinz, S., Daum, S., Meister, A., Schekman, R., Bacia, K., Briggs, J. A. G., 2013. The structure of the COPII transport-vesicle coat assembled on membranes. *eLife* 2:e00951.
39
40
41
42
43
44
45 Zuber, B., Chami, M., Houssin, C., Dubochet, J., Griffiths, G., Daffe, M., 2008. Direct visualization of the outer membrane of mycobacteria and corynebacteria in their native state. *J. Bacteriol.* 190, 5672–5680.
46
47
48
49
50
51
52
53
54
55
56
57
58

Figure Legends

Figure 1. Response of detectors based on Hessian tensor and Structure tensor. (Left) A ridge profile is shown in blue and the absolute value of the largest eigenvalue of the Hessian Tensor, i.e. second order derivative (the positive values have been set to zero as in Eq. (2)) in red. The dashed line marks the ridge point where the major eigenvalue reaches its local maximum. (Right) A function showing an edge profile in blue and the largest eigenvalue of the Structure Tensor, i.e. first order derivative, in red. The dashed line marks the edge point where the major eigenvalue reaches its local maximum. The values of the eigenvalues have been normalized to fit the range of the function.

Figure 2. Tensor Voting in 2D. (A) Model for vote casting based on a stick tensor. The voter at \mathbf{x}' is shown with its normal in green. The voxel \mathbf{x} is the receiver. The dashed arc represents the arc of a circle passing through \mathbf{x}' and \mathbf{x} , which is the most likely smooth path between these points. The orientation of the vote cast from \mathbf{x}' to \mathbf{x} is shown in red. (B) 2D stick voting field calculated for $\sigma_v = 10$. The center of the field is placed at the origin, and the normal oriented along the x-axis. The 8-shape encompasses the votes with most significant saliency. (C) Tensor voting mechanism. Votes cast from three voters (orientation vectors in green) belonging to a curve (black) are shown. The votes are cast to all voxels in the neighbourhood, while the contributions to some receivers belonging to the same curve are shown as red dotted arrows. At the end of the voting process, voxels belonging to the curve (a geometric feature) will have been strengthened, hence enhancing the feature. The other voxels will have received divergent information, which will

1
2
3
4
5
6
7
8
9 smear them out.

10
11
12 **Figure 3.** Performance of tensor voting with cryo-ET data. (Left) a slice of a
13 cryo-tomogram of a synaptic active zone. The green arrow points to a membrane
14 gap. The yellow arrows point to structures anchored to the membranes. (Right)
15 Output of our TV implementation where membranes are enhanced, the gaps are
16 filled and the membrane-attached structures are disregarded. In this example, the
17 parameters were set to $\sigma = 2$ and $\sigma_v = 10$.
18
19
20
21
22
23

24
25
26 **Figure 4.** Tensor voting applied to an experimental cryo-tomogram of a synapse.
27 (Left) a slice of the original tomogram. (Right) Output of our TV implementation,
28 with σ_v set to 7. Prior to TV, the tomogram was subjected to scale-space operation
29 with $\sigma=3$. Pixel size at the specimen level = 1.87 nm. Bar = 100 nm.
30
31
32
33
34

35
36 **Figure 5.** Local surface characterization. (A) Colormap used for descriptors
37 shown in panels B-E. Blue color corresponds to the minimum value and red to
38 the maximum. (B-D) Planarity descriptors presented in Stage 3 of the TomoSeg-
39 MemTV procedure. (B) P_s of the slice in Figure 4(Left). (C) P_p . (D) P . (E) This
40 panel is obtained by the application of the NMS detector (Eq. (3)) to the output of
41 TV (Figure 4(Right)) and it is used as the input for the computation of planarity
42 descriptors (panels B-D). When compared to (D), the higher robustness of the de-
43 scriptor P throughout the major membranes becomes apparent.
44
45
46
47
48
49
50
51
52

53 **Figure 6.** Final stages of membrane detection with TomoSegMemTV. (Left) Out-
54 put from the local membrane detector in TomoSegMemTV (Stage 5). Notice that
55
56
57
58
59
60
61
62
63
64
65

1
2
3
4
5
6
7
8
9 this output is more robust than P shown in Figure 5(D). (Center) Result after
10 thresholding (Stage 6). (Right) Result of the global analysis based on volume
11 (Stage 6): the color encodes the volume measured for every membrane according
12 with the colormap in Figure 5(A).
13
14
15
16
17

18 **Figure 7.** TomoSegMemTV applied to a cryo-tomogram of HIV-1 virions. (A)
19 Slice of the original tomogram. (B) Scale-space with $\sigma = 2$. (C) Output of the
20 local membrane detector of TomoSegMem (also known as Membrane strength,
21 presented here in Eq. (2)). (D) Final segmentation of TomoSegMem through hys-
22 teresis thresholding and global analysis based on size (Martinez-Sanchez et al.,
23 2011). The three virions are shown with different grey values that encode the size
24 of every segmented membrane. Green arrowheads point to gaps and yellow arrow-
25 heads point to spurious segmented structures apposed to membranes. (E) Output
26 of the local membrane detector of TomoSegMemTV (Stage 5 in Section 4). (F)
27 Final segmentation of TomoSegMemTV ($\sigma_v = 10$) through simple thresholding
28 and size-based global analysis. The gaps and the structures apposed have disap-
29 peared. Grey values represent the size of the segmented membrane. Pixel size at
30 the specimen level = 1.64 nm. Bar = 100 nm.
31
32
33
34
35
36
37
38
39
40
41
42
43
44

45 **Figure 8.** TomoSegMemTV applied to a tomogram of *Caulobacter Crescentus*.
46 From left to right, the panels show a slice of the original tomogram, the delineated
47 membrane and a 3D view of the segmented structure ($\sigma_v = 10$ and $\sigma = 3$). Pixel
48 size at the specimen level = 2.84 nm. Bar = 400 nm.
49
50
51
52
53
54
55
56
57
58
59
60
61
62
63
64
65

1
2
3
4
5
6
7
8
9 **Figure 9.** Segmentation by TomoSegMemTV of three different cryo-tomograms
10 of neuronal synapses. We used $\sigma_v \in [5, 10]$ and $\sigma \in [1.5, 2]$. These datasets
11 were denoised by anisotropic nonlinear diffusion prior to the segmentation. (A,B)
12 Tomogram 1, shown already on Figure 6. (A) Detection of the pre- and post-
13 synaptic membranes (green) and the **membrane regions that delineate the synaptic**
14 **cleft (red)**. Note the little effect provided by the prior use of anisotropic nonlinear
15 diffusion when compared to Figures 4 and 6. (B) Pre-synaptic cytoplasm (blue)
16 was segmented using dilation operations from a point selected by the user (see
17 panel A) and with the segmented membranes acting as boundaries. **Part of the**
18 **cytoplasm that lies within a specified distance to the synaptic cleft** is highlighted
19 in cyan. The vesicles (yellow) were detected by template matching using spheres
20 distorted by the missing wedge as references. (C-F) Tomogram 2. (C) Slice of the
21 tomogram. The arrow points to an area zoomed in (E,F). (D) Segmentation. The
22 same colors as in (A,B) are used to denote the segmented membranes and regions.
23 In violet, a mitochondrion is extracted with TomoSegMemTV configured for de-
24 tecting edge-like structures. (E) Membranes in tomograms often present holes or
25 appear blurred. Tensor Voting succeeded in bridging these gaps (F). (G,H) To-
26 mogram 3. Segmented structures use the same color code as above. The panels
27 also show the graphical user interface developed in this work. **Pixel size at the**
28 **specimen level = 1.87 nm.**
29
30
31
32
33
34
35
36
37
38
39
40
41
42
43
44
45
46
47
48

49 **Figure 10.** 3D visualization of several segmented cryo-tomograms of neuronal
50 synapses. Segmented membranes are shown in blue, **the boundaries of the synap-**
51 **tic cleft in red and** vesicles in yellow.
52
53
54
55
56
57
58

1
2
3
4
5
6
7
8
9
10
11
12
13
14
15
16
17
18
19
20
21
22
23
24
25
26
27
28
29
30
31
32
33
34
35
36
37
38
39
40
41
42
43
44
45
46
47
48
49
50
51
52
53
54
55
56
57
58
59
60
61
62
63
64
65

Figures

1
2
3
4
5
6
7
8
9
10
11
12
13
14
15
16
17
18
19
20
21
22
23
24
25
26
27
28
29
30
31
32
33
34
35
36
37
38
39
40
41
42
43
44
45
46
47
48
49
50
51
52
53
54
55
56
57
58
59
60
61
62
63
64
65

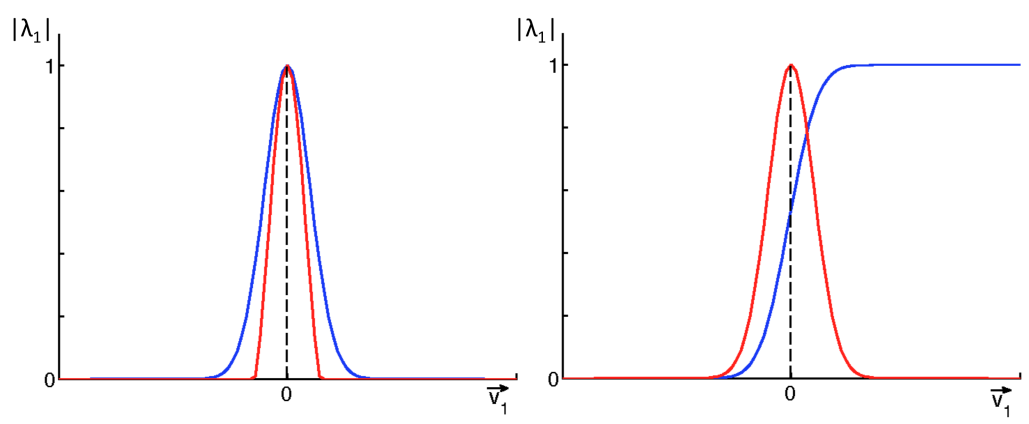


Figure 1: Response of detectors based on Hessian tensor and Structure tensor. (Left) A ridge profile is shown in blue and the absolute value of the largest eigenvalue of the Hessian Tensor, i.e. second order derivative (the positive values have been set to zero as in Eq. (2)) in red. The dashed line marks the ridge point where the major eigenvalue reaches its local maximum. (Right) A function showing an edge profile in blue and the largest eigenvalue of the Structure Tensor, i.e. first order derivative, in red. The dashed line marks the edge point where the major eigenvalue reaches its local maximum. The values of the eigenvalues have been normalized to fit the range of the function.

1
2
3
4
5
6
7
8
9
10
11
12
13
14
15
16
17
18
19
20
21
22
23
24
25
26
27
28
29
30
31
32
33
34
35
36
37
38
39
40
41
42
43
44
45
46
47
48
49
50
51
52
53
54
55
56
57
58
59
60
61
62
63
64
65

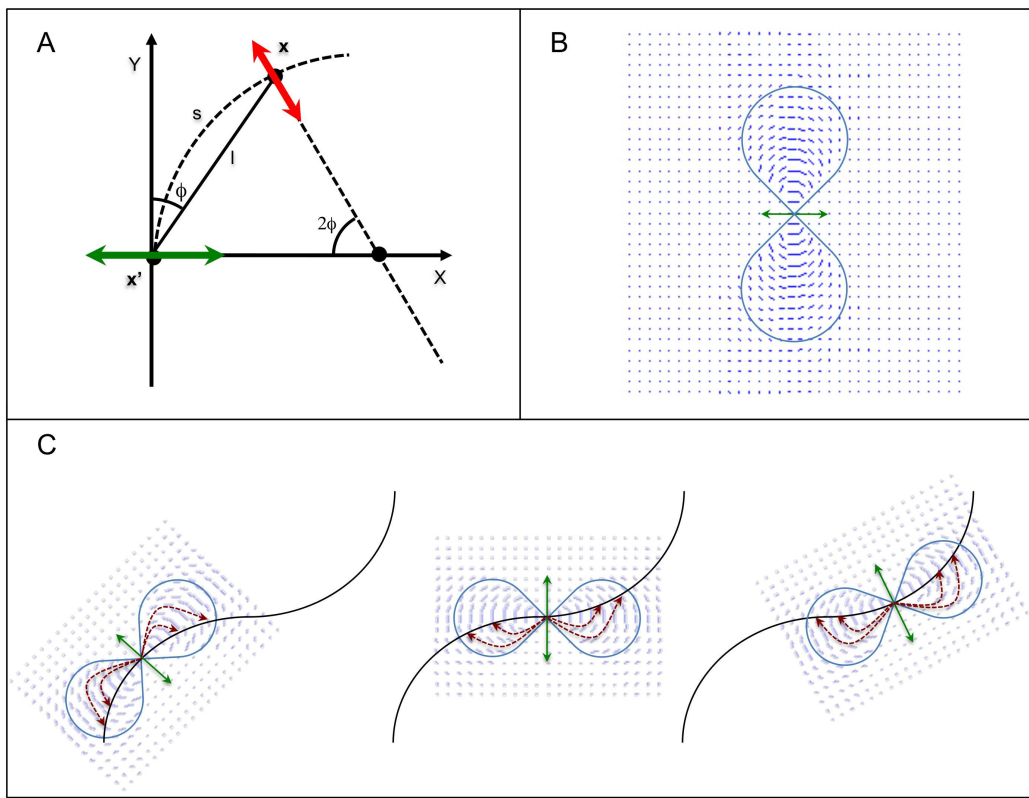


Figure 2: Tensor Voting in 2D. (A) Model for vote casting based on a stick tensor. The voter at \mathbf{x}' is shown with its normal in green. The voxel \mathbf{x} is the receiver. The dashed arc represents the arc of a circle passing through \mathbf{x}' and \mathbf{x} , which is the most likely smooth path between these points. The orientation of the vote cast from \mathbf{x}' to \mathbf{x} is shown in red. (B) 2D stick voting field calculated for $\sigma_v = 10$. The center of the field is placed at the origin, and the normal oriented along the x-axis. The 8-shape encompasses the votes with most significant saliency. (C) Tensor voting mechanism. Votes cast from three voters (orientation vectors in green) belonging to a curve (black) are shown. The votes are cast to all voxels in the neighbourhood, while the contributions to some receivers belonging to the same curve are shown as red dotted arrows. At the end of the voting process, voxels belonging to the curve (a geometric feature) will have been strengthened, hence enhancing the feature. The other voxels will have received divergent information, which will smear them out.

1
2
3
4
5
6
7
8
9
10
11
12
13
14
15
16
17
18
19
20
21
22
23
24
25
26
27
28
29
30
31
32
33
34
35
36
37
38
39
40
41
42
43
44
45
46
47
48
49
50
51
52
53
54
55
56
57
58
59
60
61
62
63
64
65

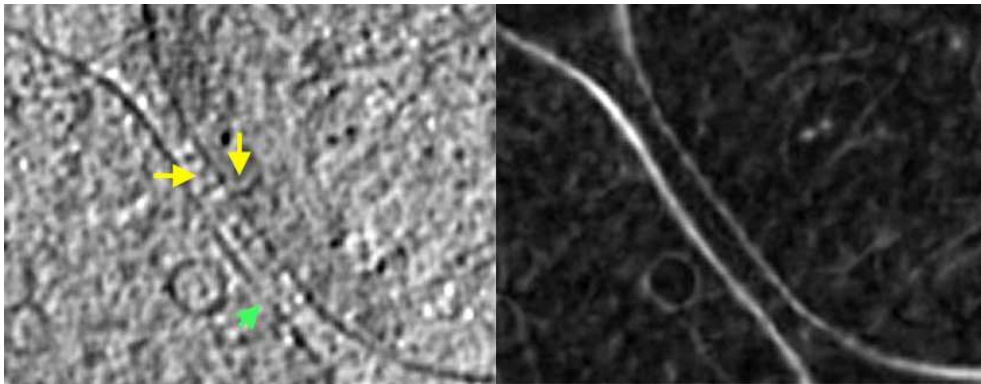


Figure 3: Performance of tensor voting with cryo-ET data. (Left) a slice of a cryo-tomogram of a synaptic active zone. The green arrow points to a membrane gap. The yellow arrows point to structures anchored to the membranes. (Right) Output of our TV implementation where membranes are enhanced, the gaps are filled and the membrane-attached structures are disregarded. In this example, the parameters were set to $\sigma = 2$ and $\sigma_v = 10$.

1
2
3
4
5
6
7
8
9
10
11
12
13
14
15
16
17
18
19
20
21
22
23
24
25
26
27
28
29
30
31
32
33
34
35
36
37
38
39
40
41
42
43
44
45
46
47
48
49
50
51
52
53
54
55
56
57
58
59
60
61
62
63
64
65

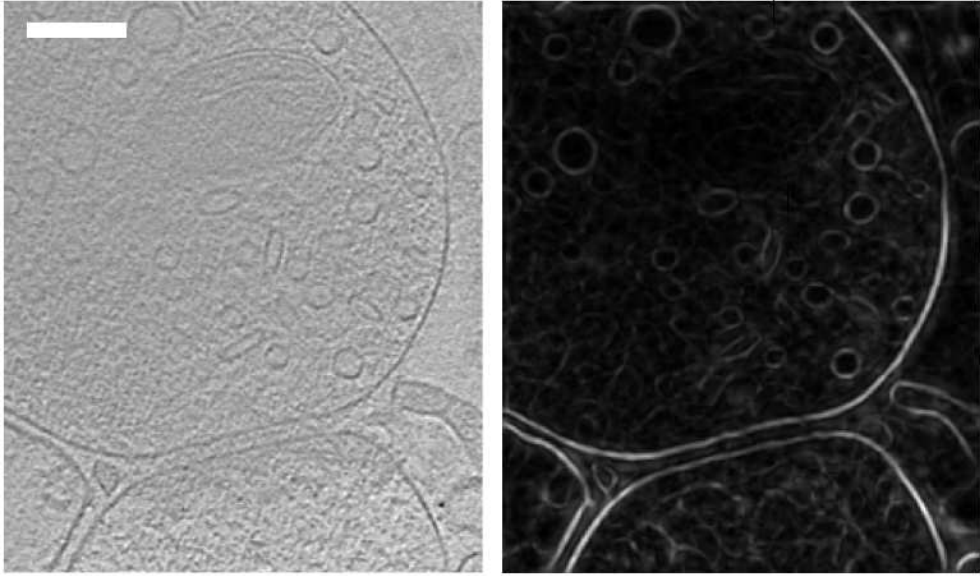


Figure 4: Tensor voting applied to an experimental cryo-tomogram of a synapse. (Left) a slice of the original tomogram. (Right) Output of our TV implementation, with σ_v set to 7. Prior to TV, the tomogram was subjected to scale-space operation with $\sigma=3$. Pixel size at the specimen level = 1.87 nm. Bar = 100 nm.

1
2
3
4
5
6
7
8
9
10
11
12
13
14
15
16
17
18
19
20
21
22
23
24
25
26
27
28
29
30
31
32
33
34
35
36
37
38
39
40
41
42
43
44
45
46
47
48
49
50
51
52
53
54
55
56
57
58
59
60
61
62
63
64
65

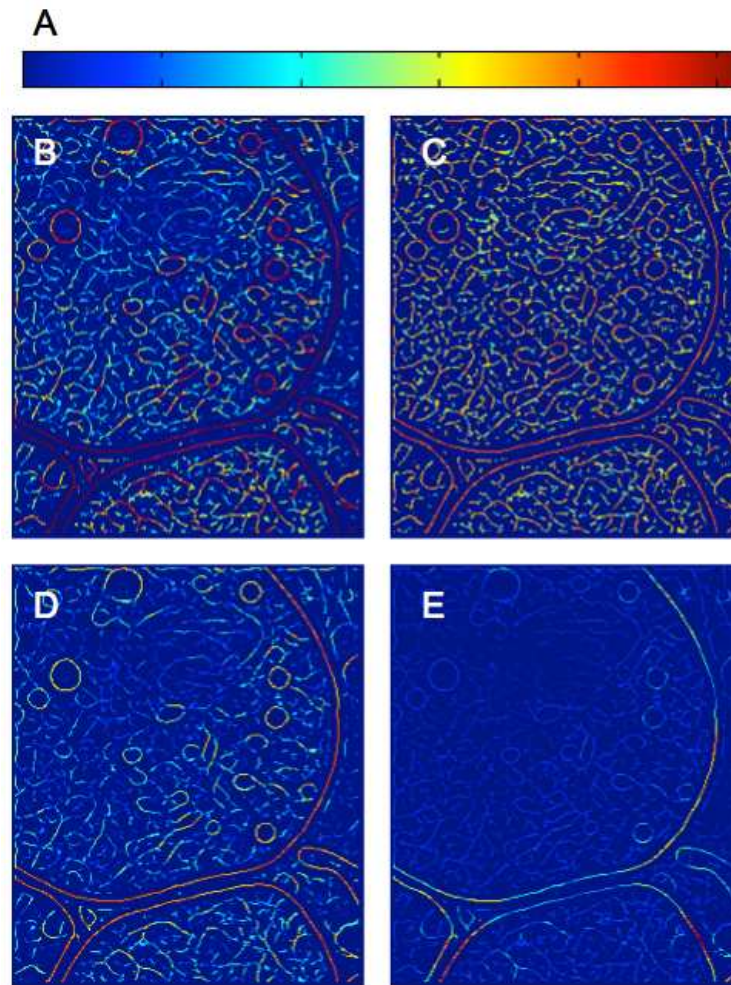


Figure 5: Local surface characterization. (A) Colormap used for descriptors shown in panels B-E. Blue color corresponds to the minimum value and red to the maximum. (B-D) Planarity descriptors presented in Stage 3 of the TomoSegMemTV procedure. (B) P_s of the slice in Figure 4(Left). (C) P_p . (D) P . (E) This panel is obtained by the application of the NMS detector (Eq. (3)) to the output of TV (Figure 4(Right)) and it is used as the input for the computation of planarity descriptors (panels B-D). When compared to (D), the higher robustness of the descriptor P throughout the major membranes becomes apparent.

1
2
3
4
5
6
7
8
9
10
11
12
13
14
15
16
17
18
19
20
21
22
23
24
25
26
27
28
29
30
31
32
33
34
35
36
37
38
39
40
41
42
43
44
45
46
47
48
49
50
51
52
53
54
55
56
57
58
59
60
61
62
63
64
65

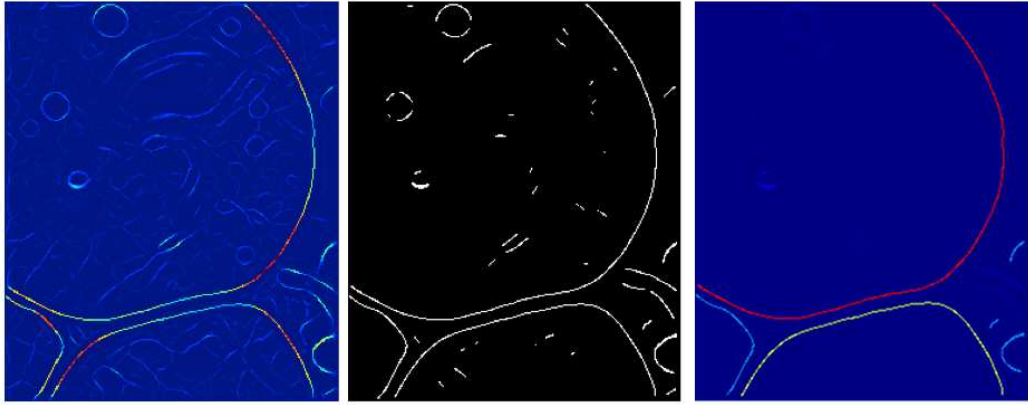


Figure 6: Final stages of membrane detection with TomoSegMemTV. (Left) Output from the local membrane detector in TomoSegMemTV (Stage 5). Notice that this output is more robust than P shown in Figure 5(D). (Center) Result after thresholding (Stage 6). (Right) Result of the global analysis based on volume (Stage 6): the color encodes the volume measured for every membrane according with the colormap in Figure 5(A).

1
2
3
4
5
6
7
8
9
10
11
12
13
14
15
16
17
18
19
20
21
22
23
24
25
26
27
28
29
30
31
32
33
34
35
36
37
38
39
40
41
42
43
44
45
46
47
48
49
50
51
52
53
54
55
56
57
58
59
60
61
62
63
64
65

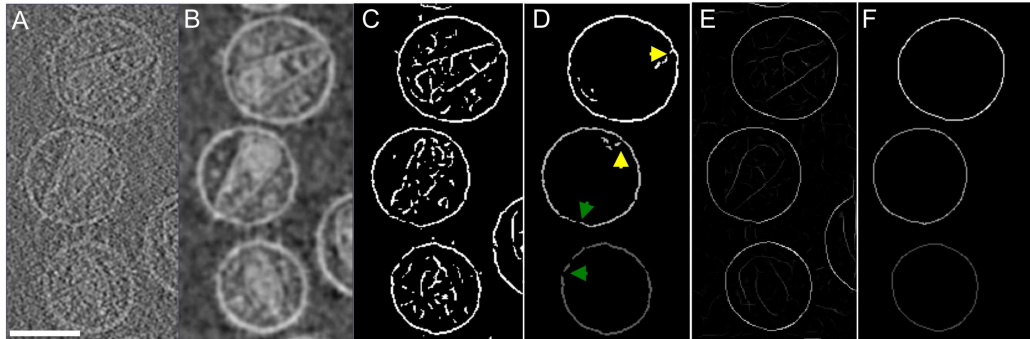


Figure 7: TomoSegMemTV applied to a cryo-tomogram of HIV-1 virions. (A) Slice of the original tomogram. (B) Scale-space with $\sigma = 2$. (C) Output of the local membrane detector of TomoSegMem (also known as Membrane strength, presented here in Eq. (2)). (D) Final segmentation of TomoSegMem through hysteresis thresholding and global analysis based on size (Martinez-Sanchez et al., 2011). The three virions are shown with different grey values that encode the size of every segmented membrane. Green arrowheads point to gaps and yellow arrowheads point to spurious segmented structures apposed to membranes. (E) Output of the local membrane detector of TomoSegMemTV (Stage 5 in Section 4). (F) Final segmentation of TomoSegMemTV ($\sigma_v = 10$) through simple thresholding and size-based global analysis. The gaps and the structures apposed have disappeared. Grey values represent the size of the segmented membrane. Pixel size at the specimen level = 1.64 nm. Bar = 100 nm.

1
2
3
4
5
6
7
8
9
10
11
12
13
14
15
16
17
18
19
20
21
22
23
24
25
26
27
28
29
30
31
32
33
34
35
36
37
38
39
40
41
42
43
44
45
46
47
48
49
50
51
52
53
54
55
56
57
58
59
60
61
62
63
64
65

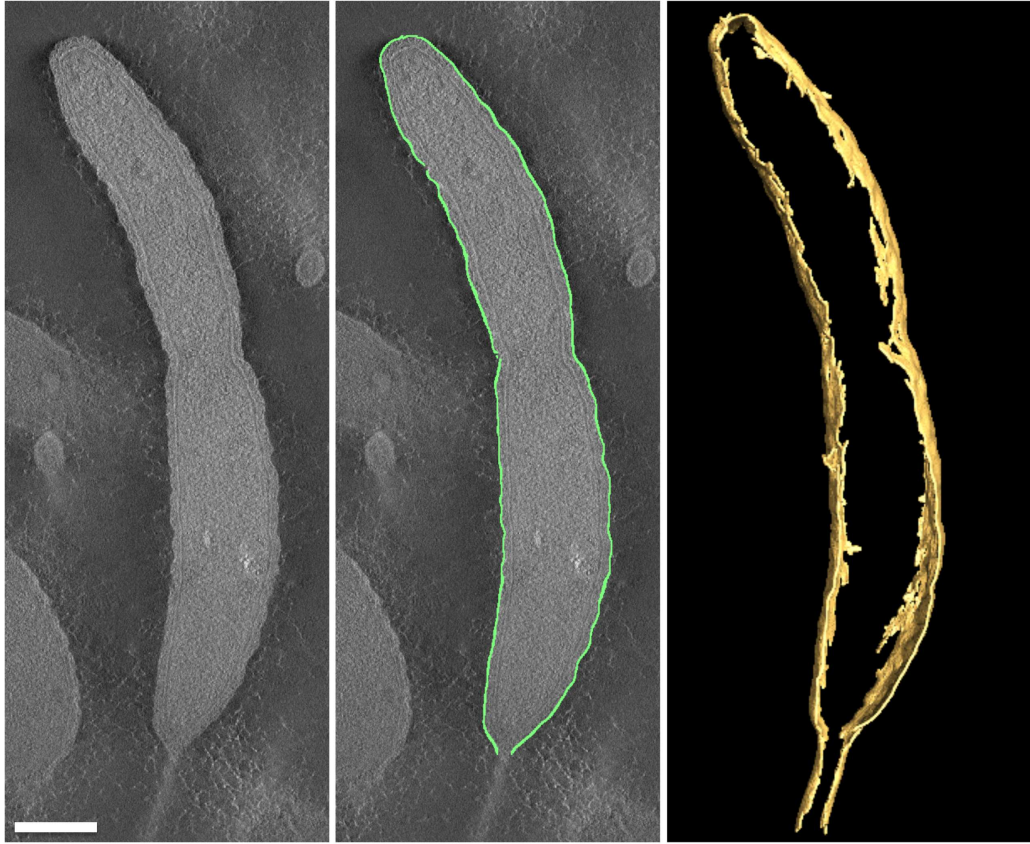


Figure 8: TomoSegMemTV applied to a tomogram of *Caulobacter Crescentus*. From left to right, the panels show a slice of the original tomogram, the delineated membrane and a 3D view of the segmented structure ($\sigma_v = 10$ and $\sigma = 3$). Pixel size at the specimen level = 2.84 nm. Bar = 400 nm.

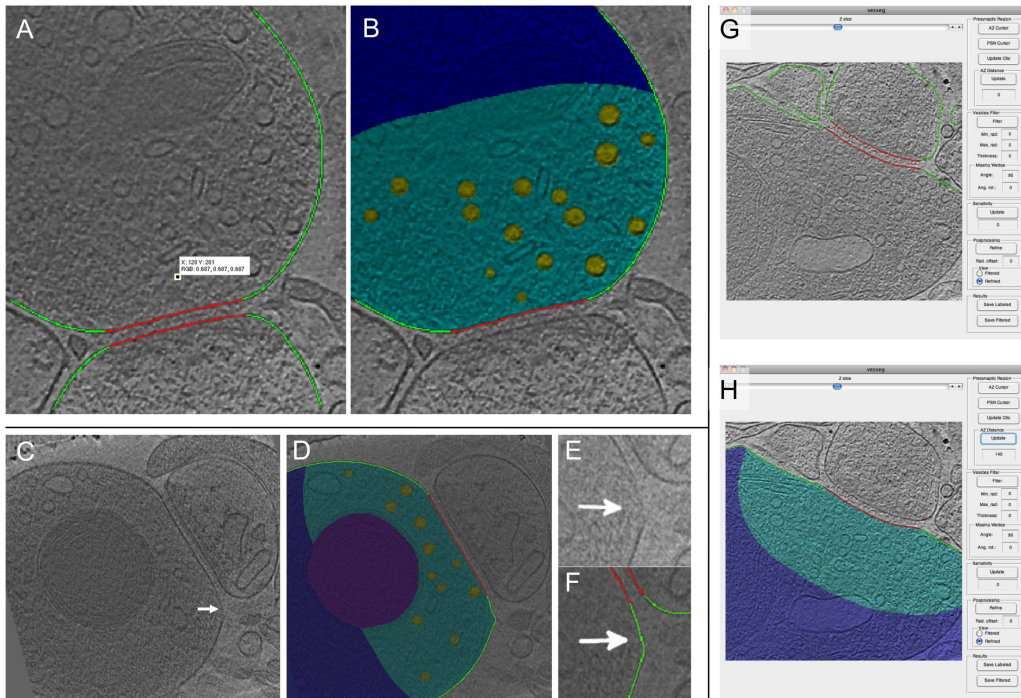


Figure 9: Segmentation by TomoSegMemTV of three different cryo-tomograms of neuronal synapses. We used $\sigma_v \in [5, 10]$ and $\sigma \in [1.5, 2]$. These datasets were denoised by anisotropic nonlinear diffusion prior to the segmentation. (A,B) Tomogram 1, shown already on Figure 6. (A) Detection of the pre- and post-synaptic membranes (green) and the **membrane regions that delineate the synaptic cleft (red)**. Note the little effect provided by the prior use of anisotropic nonlinear diffusion when compared to Figures 4 and 6. (B) Pre-synaptic cytoplasm (blue) was segmented using dilation operations from a point selected by the user (see panel A) and with the segmented membranes acting as boundaries. **Part of the cytoplasm that lies within a specified distance to the synaptic cleft** is highlighted in cyan. The vesicles (yellow) were detected by template matching using spheres distorted by the missing wedge as references. (C-F) Tomogram 2. (C) Slice of the tomogram. The arrow points to an area zoomed in (E,F). (D) Segmentation. The same colors as in (A,B) are used to denote the segmented membranes and regions. In violet, a mitochondrion is extracted with TomoSegMemTV configured for detecting edge-like structures. (E) Membranes in tomograms often present holes or appear blurred. Tensor Voting succeeded in bridging these gaps (F). (G,H) Tomogram 3. Segmented structures use the same color code as above. The panels also show the graphical user interface developed in this work. **Pixel size at the specimen level = 1.87 nm.**

1
2
3
4
5
6
7
8
9
10
11
12
13
14
15
16
17
18
19
20
21
22
23
24
25
26
27
28
29
30
31
32
33
34
35
36
37
38
39
40
41
42
43
44
45
46
47
48
49
50
51
52
53
54
55
56
57
58
59
60
61
62
63
64
65

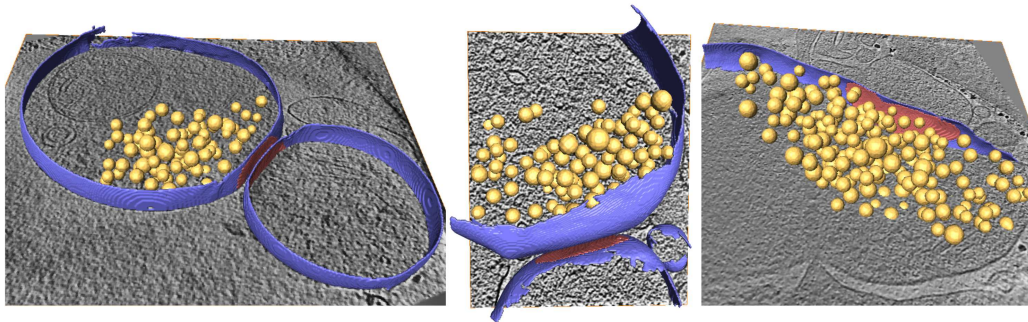


Figure 10: 3D visualization of several segmented cryo-tomograms of neuronal synapses. Segmented membranes are shown in blue, the boundaries of the synaptic cleft in red and vesicles in yellow.

1
2
3
4
5
6
7
8
9
10
11
12
13
14
15
16
17
18
19
20
21
22
23
24
25
26
27
28
29
30
31
32
33
34
35
36
37
38
39
40
41
42
43
44
45
46
47
48
49
50
51
52
53
54
55
56
57
58
59
60
61
62
63
64
65

Tables

1
2
3
4
5
6
7
8
9
10
11
12
13
14
15
16
17
18
19
20
21
22
23
24
25
26
27
28
29
30
31
32
33
34
35
36
37
38
39
40
41
42
43
44
45
46
47
48
49
50
51
52
53
54
55
56
57
58
59
60
61
62
63
64
65

Table 1: Quantitative analysis based on synthetic phantom for TomoSegMemTV.

	1000 Ribosomes			5000 Ribosomes			10000 Ribosomes		
SNR	PR	TPF	TNF	PR	TPF	TNF	PR	TPF	TNF
0.05	0.8434	0.9167	0.9947	0.8266	0.9096	0.9941	0.7193	0.8306	0.9906
0.1	0.8474	0.9231	0.9946	0.8332	0.9116	0.9938	0.8004	0.8915	0.9925
2	0.8487	0.9274	0.9939	0.8487	0.9274	0.9939	0.8373	0.9178	0.9937

Table 2: Quantitative analysis based on synthetic phantom for Template Matching.

	1000 Ribosomes			5000 Ribosomes			10000 Ribosomes		
SNR	PR	TPF	TNF	PR	TPF	TNF	PR	TPF	TNF
0.05	0.7538	0.8524	0.9921	0.6440	0.7639	0.9878	0.3953	0.4753	0.9867
0.1	0.7640	0.8769	0.9903	0.6859	0.8209	0.9871	0.4671	0.5300	0.9911
2	0.7766	0.8655	0.9932	0.6920	0.8158	0.9882	0.5460	0.6324	0.9896